Mismatch loss in bifacial modules due to non-uniform illumination in 1D tracking systems

Keith R. McIntosh,[1] Malcolm D. Abbott,[1] Benjamin A. Sudbury[1] and Jenya Meydbray[2]

[1]PV Lighthouse, Coledale, NSW 2515, AUSTRALIA
[2]PV Evolution Labs (PVEL), Berkeley, CA 94710, USA

***Abstract*— We apply ray tracing to compute the light-generated current I_L within each solar cell of a bifacial tracking module, and SPICE modelling to quantify how the spatial variability in I_L (i.e., current mismatch) reduces the module's output power P_{MP}. We find that 10 million rays are required to accurately map I_L for a central module in a PV system at a given insolation condition. The relative reduction in P_{MP} is found to be (i) greatest in the middle of the day for sunny conditions, (ii) independent of time for very cloudy conditions, (iii) higher for edge modules than central modules, (iv) higher for one-high portrait configurations than for two-high, and (v) higher when the ground albedo is higher. We trace 2 billion rays on 2000 parallel cores to solve a module's annual energy yield for a system located at Golden CO with a sandy soil. The yield reduction in a one-high configuration due to non-uniform illumination is 0.23% for a central module and 0.35% for an edge module. Thus, in this example, mismatch loss due to non-uniform illumination within an individual tracking module is relatively low, even when the rear of the module is shaded by a torque tube.**

I. Introduction

The illumination incident to the rear of a bifacial module is much less uniform than the illumination incident to the front. Major sources of non-uniformity are the variable distance from the ground to the cells, shading patterns on the ground from the modules and system components, and, in the case of tracking modules, shading from the torque tube [1]–[7]. As will be seen, the non-uniformity is greater for modules nearer the ground, and for modules at the edge of a system.

Predicting the rear illumination and the resulting energy yield is not trivial. As well as the sources of non-uniformity, reflection from the ground reduces the intensity and modifies the spectrum, scattering from the ground leads to a large distribution of incident angles, and all of these effects depend on the time of day and year, the ratio of direct to diffuse light, and any tracking algorithms applied to the module. Moreover, cells have different angular and specular responses under front and rear illumination, they operate at variable temperatures depending on the weather and insolation, and non-uniform illumination leads to current mismatch that reduces module power.

Previous studies have incorporated a variety of these effects. The optical behavior of bifacial systems has been evaluated with ray tracing [1], [7]–[10] and view factor models [2]–[7], [11]–[14], some down to the resolution of illumination per cell [1], [2], [9]; and the optical outputs have been combined with electrical and temperature models [1], [2], [13], [15]. To date, however, no investigation has been performed to a sufficient level of detail to quantify how the illumination non-uniformity affects current mismatch and hence power loss.

In this work, we take all of the aforementioned effects into consideration except for shading from posts. Raytracing is performed on 2000 parallel cores in the cloud—a veritable super computer—to trace rays from the system level to the micron level, accounting for spectra, diffuse and direct light, spectral albedo, backtracking, and torque tubes to determine the light-generated current I_L in each cell of a module on a 1D tracking bifacial system. SPICE modelling is then used to determine how the variability in I_L contributes to a reduction in power, accounting for temperature with the Faiman model [16]. We describe the trends and compute an example output and mismatch loss for a 1D tracking module in one-hourly intervals over a year at Golden CO using real weather data.

II. Simulation Inputs

2.1 Module inputs

Fig. 1 presents a schematic of the PV module examined in this work. It represents a modern frameless glass–glass bifacial module with 72 solar cells. Table I presents the module's IV characteristics under standard test conditions (STC), which is 25 °C and the spatially uniform, normally

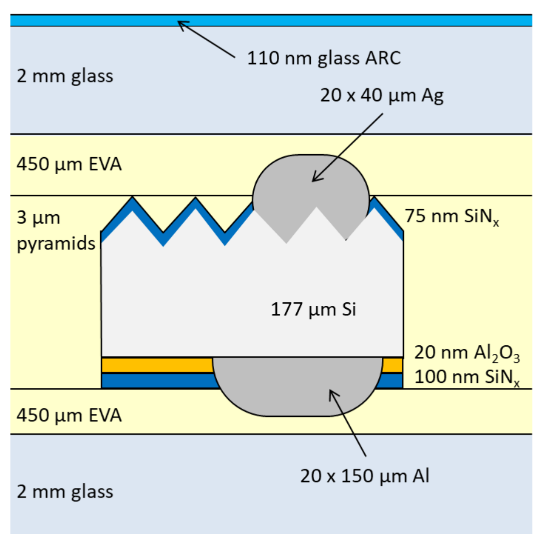

Fig. 1. Features and dimensions of the bifacial module (not to scale).

incident AM1.5g spectrum. Appendix A provides the many inputs used to simulate the module with SunSolve™ [17].

The simulations that follow assume that there is no soiling on the modules, that there is no spatial variation of any material, that all solar cells within the module are identical, that the contacts that connect the tabs (at the top and bottom of the module) do not affect the optical behavior of the module, that the modules are frameless, and that the optical properties are independent of temperature.

Table I. Simulated IV outputs at STC.

Illuminated side	**I_{SC} (A)**	**V_{OC} (V)**	**P_{MP} (W)**
Front	9.50	47.5	360
Rear	7.33	47.1	277

2.2 Optimal number of rays

If we could trace infinitely many rays at STC, the illumination incident to each cell and hence I_L would be identical. This is because the incident illumination is spatially uniform, the cell properties are identical, and there is no backsheet between cells redirecting more light to the edge cells (as occurs in monofacial modules [18], [19]). Since SunSolve traces a finite number of rays, and since each ray begins at a random location above the module, some cells must receive more rays than others, leading to a variable I_L. Naturally, the resulting random error decreases as the number of rays increases.

Our objective was to trace only the number of rays for which I_L variability due to the random nature of the Monte Carlo simulation reduced the output power P_{MP} by ≤ 0.1%. We determined that number by simulating the module at STC, where the number of rays varied from 1000 to 10 million. Figs. 2–4 present the results.

4.8%	-2.4%	0.5%	1.7%	0.2%	0.1%
-1.3%	-1.0%	-1.0%	-3.3%	2.6%	1.8%
0.7%	3.9%	1.2%	0.3%	-4.2%	-0.8%
-2.6%	2.8%	0.9%	-1.2%	5.2%	-4.4%
-2.4%	-1.1%	3.6%	-5.0%	3.5%	-9.4%
1.7%	-0.7%	3.1%	2.6%	-5.0%	1.6%
-3.1%	-0.2%	0.6%	-1.5%	-0.6%	1.2%
-0.9%	-3.0%	-4.1%	-3.6%	2.7%	4.7%
2.1%	6.1%	-1.3%	-4.8%	1.9%	2.0%
3.8%	5.4%	-4.8%	0.7%	1.0%	-1.4%
-2.3%	-2.4%	-1.4%	-0.5%	3.7%	-4.2%
1.9%	3.0%	-3.8%	2.4%	-1.0%	2.4%

Fig. 2. Variability in I_L for each cell within a module under front illumination at STC with 100,000 rays.

Fig. 2 maps the variability in I_L for just 100,000 rays. The random variability in I_L is significant, varying by about ±8% across the module. Fig. 3 plots the module's IV curves, which exhibit kinks due to the I_L variability (i.e., to current mismatch), showing how the error decreases as the number of rays increases. Fig. 4 plots (a) the resulting P_{MP} and (b) the relative underestimation in P_{MP} due to insufficient rays.

From Fig. 4(b) we can conclude that 3 million rays are sufficient to reduce the underestimation in P_{MP} to ~0.1%. Since the module area comprises ~30% of the unit system area, the following simulations trace 10 million rays per module within a unit system.

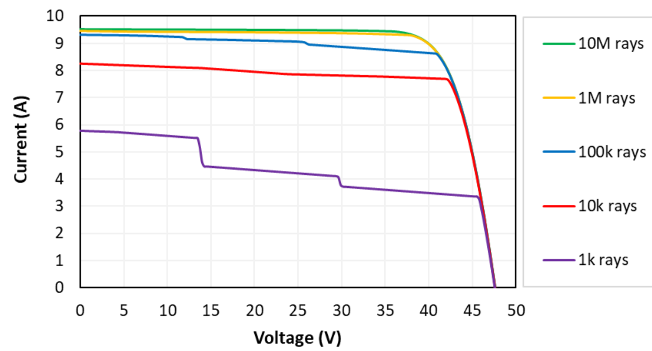

Fig. 3. IV curves at STC for various numbers of rays traced.

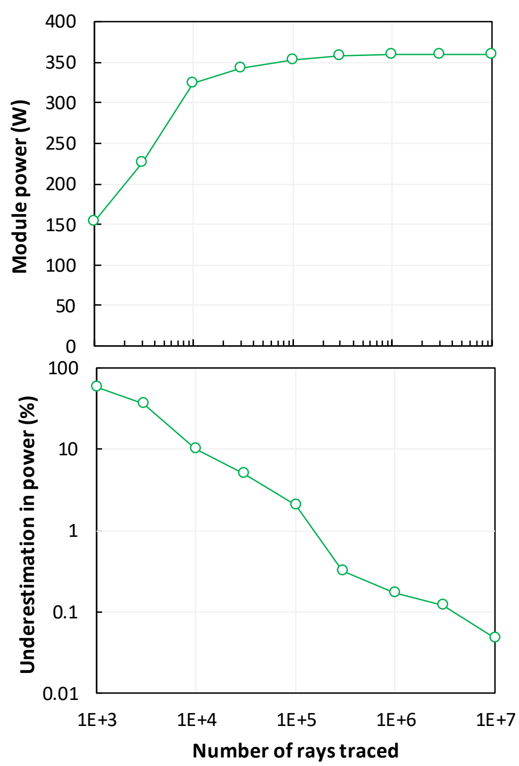

Fig. 4. (a) P_{MP} (b) underestimation of P_{MP} vs number of rays.

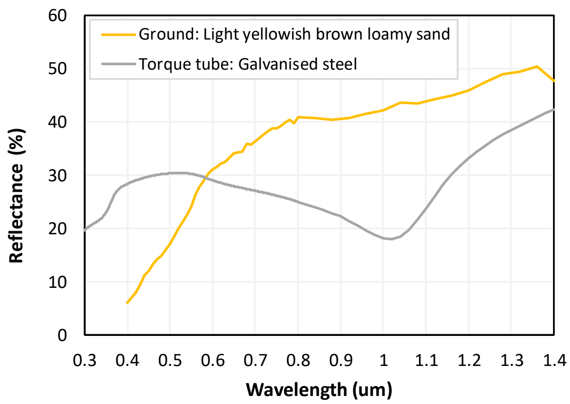

Fig. 5. Reflectance of the ground and torque tube.

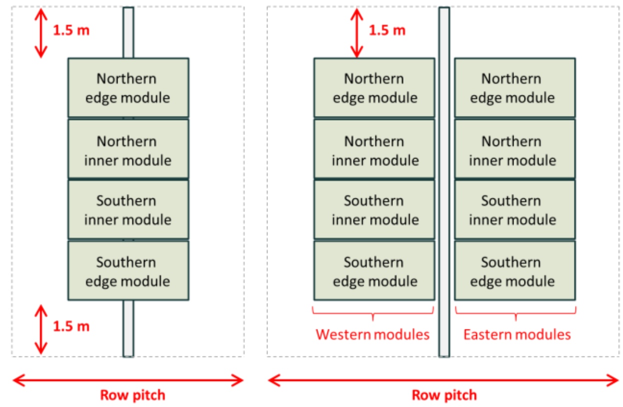

Fig. 6. Plan view of the unit system for (a) one-high (b) two-high systems when edge modules are investigated.

2.3 System inputs

We assess two common 1D tracking bifacial configurations: (i) a 'one-high' portrait configuration (like [6]) and (ii) a 'two-high' portrait configuration. The names of these configurations define the number of modules connected to the torque tube in the EW direction. The dimensions are estimates for a typical modern installation.

For both configurations the torque tube is aligned NS, has the reflectance plotted in Fig. 5 (galvanized steel [20]), and is treated as a partial scatterer (50% specular, 50% Lambertian); the ground is flat, has the spectral albedo plotted in Fig. 5 (light-yellowish-brown loamy sand [20]), and is treated as an ideal scatterer (100% Lambertian); the albedo is assumed constant with time, despite this being a poor assumption [21]; and the trackers have a maximum tilt of 60° and backtrack to ensure there is no row-to-row shading at any time of day [4].

The one-high configuration has a row pitch of 5 m, equivalent to a ground-coverage ratio of GCR = 39.4%. Its modules are not separated in the NS direction and its torque tube is 1.2 m above the ground, 7.5 cm below the panels, and has a diameter of 12.7 cm.

The two-high configuration has a row pitch of 9 m, equivalent to a GCR of 45.9%. Its modules are separated by 20 cm in both the EW and NS directions and its torque tube is 2.25 m above the ground, 5 cm below the panels, and has a square cross section of dimensions 10 cm × 10 cm.

The central modules of a PV system are examined by simulating a unit system within an infinite field. Thus, the unit system for a central module contains one module for the one-high configuration and two modules for the two-high configuration.

Edge modules are examined by simulating the unit systems shown in Fig. 6 within an infinite field. These unit systems consist of a short sub-row of four modules separated from the next sub-row by a gap of 3m. As will be seen in Section 3.5, we need more than four modules to ensure that the innermost modules are not affected by the edges, but nevertheless, we can still adequately quantify cell mismatch in edge modules.

2.4 Insolation and weather inputs

We apply the insolation and weather data recorded by NREL at Golden CO between 1-Sep-2017 and 31-Aug-2018. This includes ambient temperature, wind velocity, solar zenith and azimuth, as well as the direct perpendicular intensity and spectrum, and global horizontal intensity and spectrum. The data was downloaded from NREL [22] and prepared in the manner described in Appendix B.

2.5 Computations

Each configuration was solved with 10 million rays per unit system for both direct and diffuse light at 100 different incident angles. This amounts to 2 or 4 billion rays for one-high and two-high configurations. Solving the resulting SPICE solutions twice for each solar cell (independent and in series to determine mismatch loss) for a 12-month period in one-hourly intervals amounts to 2 × 72 × 4369 = 633,024 IV curves per module. Thus, the computation of an annual yield requires serious computational power, which PV Lighthouse harnesses through the cloud.

III NON-UNIFORMITY IN BIFACIAL SYSTEMS

The purpose of this work is to assess the illumination non-uniformity on a tracking bifacial panel, and to quantify its impact on mismatch loss. Before presenting the results, we first describe the major sources of non-uniformity.

There is very little non-uniformity on the front of the modules because both (i) row-to-row shading and (ii) reflection from the ground onto the front are minimal. Row-to-row shading of direct light is prevented entirely by the backtracking and, in general, is minimal for diffuse light because it only affects high-angle diffuse light when the modules are tilted. Reflection from the ground is also largely prevented by tracking the modules (except when the row pitch is very large). In short, practically all of the non-uniformity occurs on the rear of the modules.

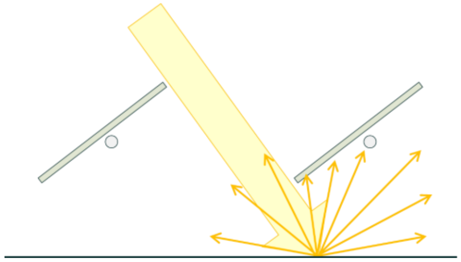

Fig. 7. Diagram showing how direct light passing between the modules reflects from the ground for the one-high configuration. This leads to a higher insolation on the cells nearest the ground and shading from the torque tube.

Fig. 7 illustrates how non-uniformity on the rear arises from direct light. Light reflecting upwards from the ground is (i) more intense on the cells nearest the ground, and (ii) shaded by the torque tube from reaching some cells near the middle of the module.

By contrast, the diffuse (isotropic) light is incident to the ground—and thence to the rear of the module—at all angles and we see little dependence on module orientation. We also find that torque tube shading is much more significant for diffuse than direct illumination.

IV RESULTS

3.1 Representative days

We select two days to illustrate the influence of direct and diffuse insolation: 6-Mar-2018, a sunny day in late winter, and 6-Apr-2018, a very cloudy day in early spring. Fig. 8 presents the direct and diffuse insolation on those days, as well as the resulting P_{MP} from a single central module in the one-high configuration.

Fig. 8(a) shows that P_{MP} is high on the sunny day, being approximately symmetric about midday and having maxima around 9 am and 3 pm. As expected for a 1D tracking system aligned NS, there is a small dip in P_{MP} between 9 am and 3 pm due to the sunlight's incident angle to the module θ_{inc} increasing until midday and decreasing afterwards.

Fig. 8(b) shows that on a very cloudy day, when there is practically no direct light at all, P_{MP} is approximately linearly dependent on the global intensity, which is entirely diffuse.

3.2 I_L uniformity — central module, one-high configuration

Figs. 9 and 10 map the relative difference in I_L of each cell at different times on the sunny and cloudy days. They show how the illumination intensity varies across the module.

On the sunny day (Fig. 9) when ~90% of the sunlight is direct, we observe the following:

- At 8 am and 4 pm, the module has a high tilt and practically no direct light falls on the ground; there is little non-uniformity at these times.

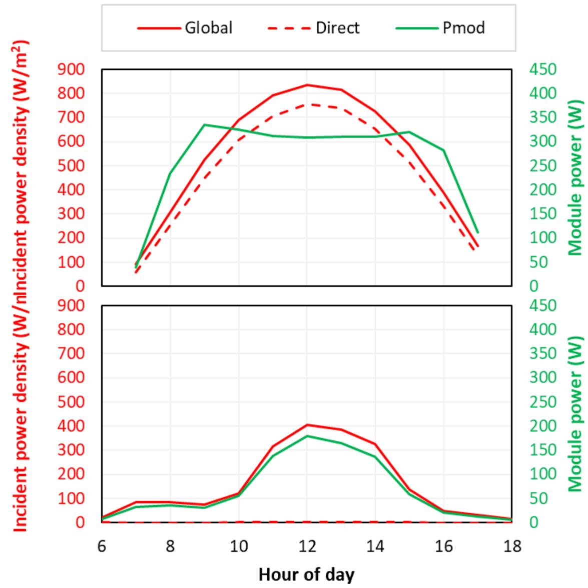

Fig. 8. Representative days: (a) 6-Mar-2018, a sunny day with no clouds, and (b) 6-Apr-2018, a cloudy day with no direct insolation.

- At 10 am and 2 pm, the module has a moderate tilt, some light is incident to the ground and the cells nearest the ground have the highest I_L. Torque tube shading is also evident—but only a little. (This finding is approximately consistent with [6], which predicted a 15% reduction in rear illumination under the torque tube, amounting to only a few percent reduction in total illumination.)
- At midday, the module is horizontal and the non-uniformity is symmetric and smaller than at 10 am and 2 pm; cells nearest the edge still have a higher I_L than in the middle.

On the very cloudy day (Fig. 10), when 100% of the light is diffuse, the non-uniformity is roughly symmetric throughout the day. The insolation in the middle of the module is lowest due to (a) torque tube shading and (b) it being furthest from the ground between the modules, which is where most light falls. The effect of (b) must be minimal because there is little or no dependence on module tilt.

Hence, on sunny days, when the incident solar power is greatest, non-uniformity is primarily due to sunlight incident to the ground reflecting onto cells nearest the ground; whereas on cloudy days, which contribute less to annual yield due to the low solar insolation, non-uniformity is primarily due to torque tube shading.

Note that the non-uniformity would be much higher early and late in the day if backtracking were not implemented to prevent row-to-row shading.

3.3 Mismatch — central module, one-high configuration

Mismatch loss for the one-high configuration is relatively small for our example scenario. It amounts to a reduction in annual yield of 0.23%. Fig. 11 plots the reduction in P_{MP} that

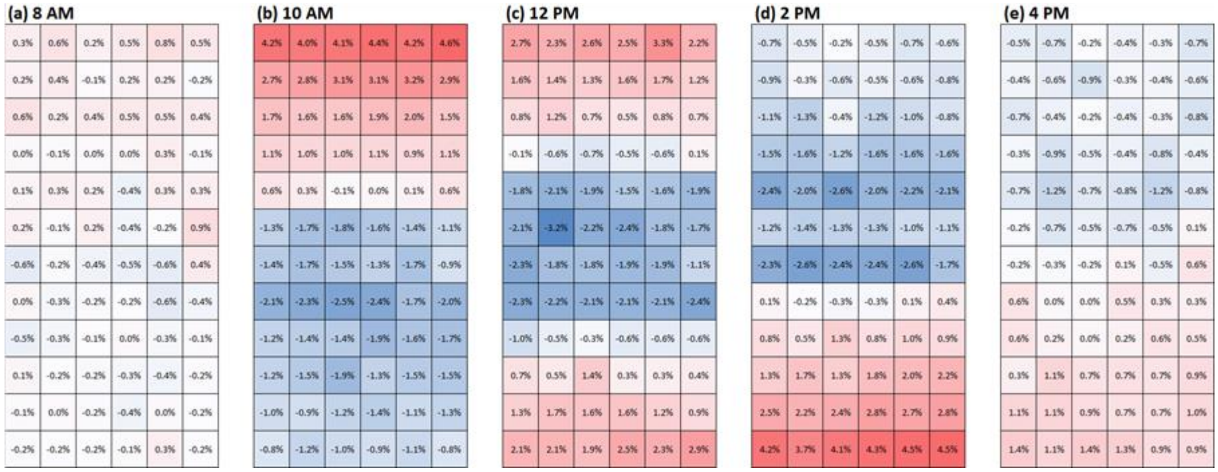

Fig. 9. Relative difference in I_L from the average for the one-high configuration on a sunny day, 6-Mar-2018.

Fig. 10. Relative difference in I_L from the average for the one-high configuration on a cloudy day, 6-Apr-2018.

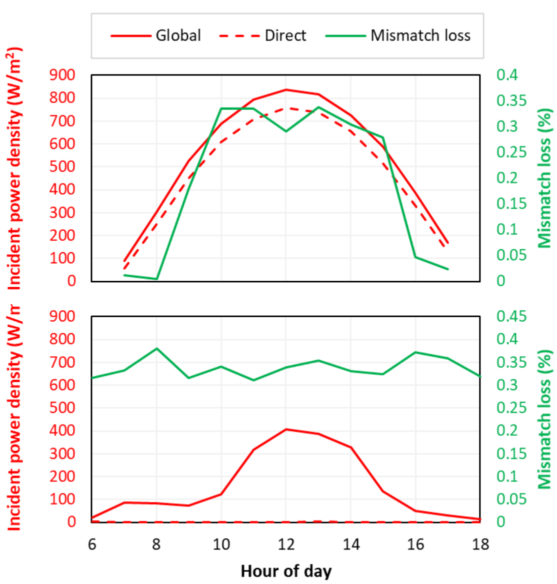

Fig. 11. Representative days: (a) 6-Mar-2018, a sunny day with no clouds, and (b) 6-Apr-2018, a cloudy day with no direct insolation.

arises due to mismatch from non-uniformity within a single module. Remember that all cells are assumed identical, so additional mismatch would result from variability in cell performance (although this has little impact in a modern module [23]).

Consistent with the observations of I_L variability in Section 3.2, we see that the mismatch loss on a sunny day is greatest during the middle of the day, and that mismatch loss on a cloudy day is similar throughout the day.

With Fig. 12, we plot the mismatch loss against the fraction of light that is direct for each day of the year. For all but the cloudiest of days, the mismatch loss is between 0.2–0.3%, and on very cloudy days, it increases to 0.3–0.4%.

3.4 Mismatch — central module, two-high configuration

The annual mismatch loss for the two-high configuration was determined to be 0.09%, significantly lower than for the one-high mismatch loss (0.23%). This is because (i) the modules are, on average, higher above the ground and hence the scattered light reflected from the ground is more uniformly

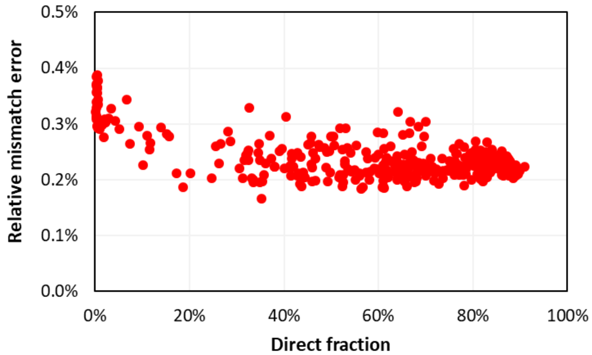

Fig. 12. Relative mismatch error vs direct fraction for central one-high module, where each symbol is one day of the year.

distributed, (ii) the non-zero spacing between modules allows more light onto the ground beneath the module, and (iii) there is minimal torque tube shading since the torque-tube is position between the two modules.

Fig. 13 plots the cell mismatch on the representative days. Similar to the one-high configuration, mismatch in the two-high configuration is variable on the sunny day and approximately constant for the cloudy day. The cell mismatch loss is greater for the module nearest to the ground.

3.5 Mismatch — edge modules

We now present the results for the simulation with four modules in a sub-row (refer to Fig. 6). Fig. 14 maps I_L variability of the one-high four-module configuration on the sunny day, and Fig. 15 plots the annual yield and mismatch loss for each year. In these simulations, every module is assumed to operate at its P_{MP} (and hence we do not assess module-to-module mismatch). We make the following observations:

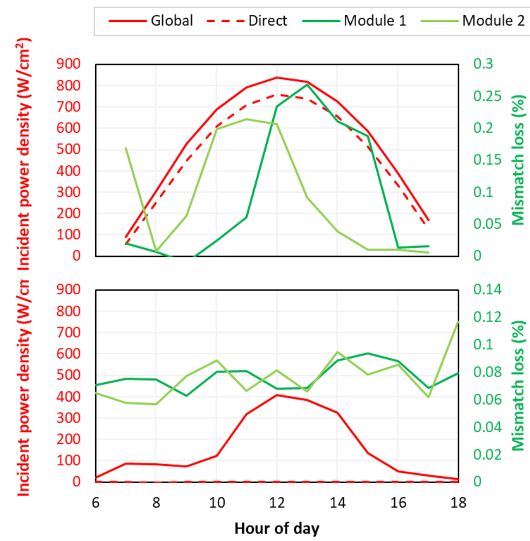

Fig. 13. Representative days: (a) 6-Mar-2018, a sunny day with no clouds, and (b) 6-Apr-2018, a cloudy day with no direct insolation.

- Southern edge modules have the highest yield, consistent with the findings of [4], [6]. In this case, they yield 3.6% and 3.2% more energy than the central module for one-high and two-high configurations, respectively. Southern modules have the highest yield because (i) being near an edge, more light is reflected from the ground to their rear, and (ii) being at the southern end of the row, the ground under the module is the least shaded by neighboring modules.
- The northern edge module also has a higher yield than its neighbor [4], [6]. Being near the edge, more light is reflected from the ground to its rear. This advantage is greatest in summer, which is when the sun's zenith angle is

(a) Northern edge

0.2%	0.5%	0.2%	0.1%	-0.2%	0.4%
-0.5%	-0.7%	-0.6%	-1.1%	0.2%	-1.3%
-1.8%	-0.7%	-2.3%	-1.9%	-1.8%	-2.5%
-2.4%	-2.3%	-2.1%	-2.7%	-2.6%	-2.4%
-4.0%	-4.3%	-4.7%	-3.7%	-4.5%	-3.5%
-4.3%	-5.1%	-5.1%	-4.6%	-5.7%	-3.7%
-4.3%	-4.2%	-4.1%	-5.7%	-4.2%	-4.9%
-4.6%	-4.6%	-4.3%	-4.1%	-6.0%	-4.1%
-2.4%	-3.3%	-2.9%	-2.9%	-3.4%	-2.3%
-2.1%	-1.5%	-2.0%	-2.5%	-1.5%	-2.0%
-0.6%	-0.4%	-0.5%	-1.9%	-0.3%	-1.5%
-0.2%	0.2%	0.1%	0.7%	-0.2%	0.6%

(b) Northern inner

0.9%	1.7%	1.1%	0.4%	1.4%	1.1%
0.0%	-0.2%	-0.2%	-0.3%	0.0%	0.4%
-2.5%	-1.3%	0.1%	-1.0%	0.7%	0.0%
-0.9%	-2.9%	-3.3%	-1.8%	-1.7%	-1.9%
-4.4%	-3.9%	-3.8%	-3.3%	-2.8%	-3.5%
-4.6%	-4.5%	-4.1%	-4.1%	-4.2%	-3.8%
-4.4%	-5.1%	-4.6%	-3.4%	-3.8%	-3.2%
-4.4%	-5.1%	-3.9%	-3.1%	-3.1%	-2.5%
-2.9%	-3.3%	-2.0%	-1.4%	-2.4%	-2.1%
-1.7%	-0.3%	-1.6%	-0.4%	-0.1%	0.1%
-0.9%	-0.2%	-0.9%	0.6%	-0.3%	1.6%
0.7%	0.8%	-0.5%	0.3%	1.7%	0.8%

(c) Southern inner

1.1%	2.3%	2.6%	2.3%	4.0%	3.6%
1.2%	2.2%	1.8%	2.6%	3.2%	4.3%
-0.1%	1.1%	1.7%	2.3%	2.3%	2.9%
0.3%	-0.1%	0.7%	0.4%	1.5%	3.1%
-3.1%	-2.5%	-1.3%	-0.4%	-0.2%	1.0%
-2.6%	-3.2%	-2.4%	-2.6%	-2.0%	-1.7%
-4.3%	-4.3%	-1.7%	-2.9%	-2.2%	-0.6%
-2.5%	-2.2%	-0.9%	-0.6%	0.8%	0.4%
-0.7%	-0.8%	0.9%	0.4%	2.0%	2.2%
0.2%	-0.2%	1.4%	1.4%	3.1%	2.5%
0.2%	1.3%	1.7%	2.6%	3.8%	2.4%
1.6%	1.5%	1.6%	3.5%	2.8%	4.1%

(d) Southern edge

4.8%	5.4%	5.4%	4.4%	6.2%	6.0%
4.1%	3.9%	4.4%	5.3%	5.8%	5.7%
3.4%	4.5%	3.6%	4.8%	5.1%	5.1%
2.9%	3.0%	4.0%	4.3%	4.2%	4.9%
1.1%	1.9%	2.7%	2.5%	4.1%	4.0%
-1.4%	-0.5%	-1.5%	-0.9%	-0.4%	2.0%
-1.2%	-0.3%	-1.0%	-1.0%	0.4%	2.2%
1.1%	1.0%	2.1%	2.8%	3.0%	2.9%
3.1%	3.0%	3.0%	4.2%	4.2%	4.6%
2.9%	4.9%	3.6%	4.9%	5.8%	5.1%
5.4%	3.2%	4.8%	4.8%	5.0%	5.2%
3.8%	4.5%	4.1%	5.6%	5.2%	5.5%

Fig. 14. Relative difference in I_L from the average of all cells in a four-module substring. One-high configuration, sunny day, 6-Mar-2018.

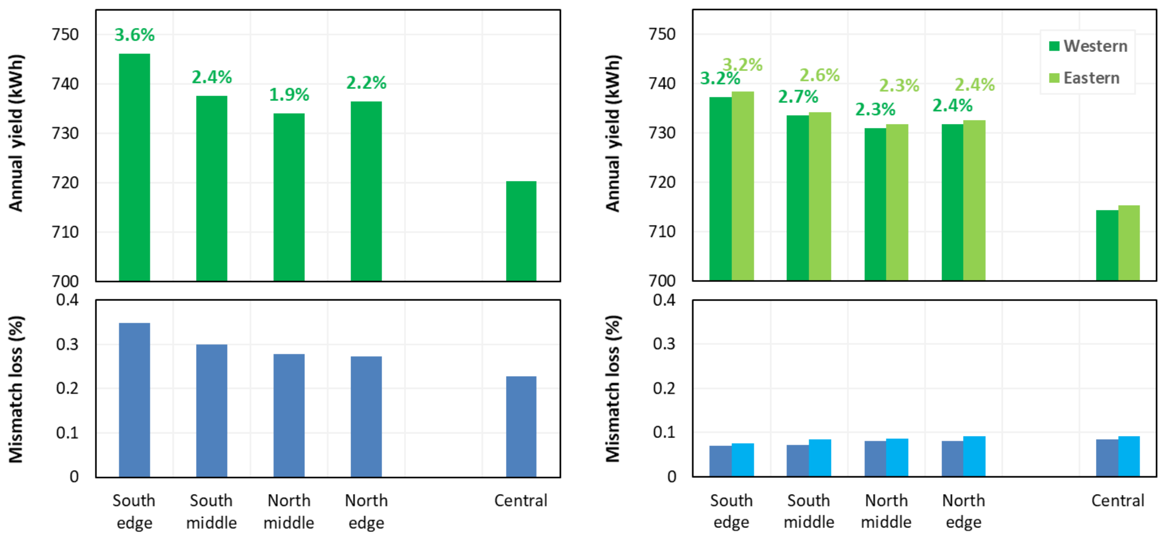

Fig. 15: (top) Annual energy yield and (bottom) mismatch loss from each module for the (left) one-high and (right) two-high systems. Remember, in this study, all modules are operating independently, and the mismatch loss only represents the loss due to current mismatch within a single module—not the mismatch loss of the row or system.

higher [4].

- The inner modules have a lower yield than the edge modules but remain superior to the central module. We therefore need to simulate more modules in a row to ensure the innermost module is unaffected by the edges. Palaez *et al.* found that 10 modules in a row were required before rear illumination on the inner modules is <5% that of the central modules in an infinitely large tracking bifacial system [6].
- There is greater cell mismatch at edge modules than central modules for the one-high configuration (up to 0.35% annual loss),
- Mismatch loss remains low for all modules in the two-high configuration (<0.1% annual loss).

3.6 Mismatch — albedo

It is clear from the above discussion that mismatch depends strongly on reflection from the ground, and hence a higher albedo must lead to a higher mismatch. Under the extreme case of frost covering the ground, for which the albedo exceeds 80% over the range 300–1200 nm [20], the annual mismatch loss for a central module increases from 0.23% to 1.37% for a one-high configuration and from 0.09% to 0.51% for a two-high configuration.

IV Conclusion

A bifacial 1D tracking system was simulated to quantify the non-uniformity of the illumination and its impact on mismatch loss within a module. It was shown how the mismatch depends on direct and diffuse light, time of day, and albedo. For our example scenarios, the reduction in annual yield for a central module (always held at P_{MP}) was small, being 0.23% for a one-high configuration and 0.09% for a two-high configuration. The loss increased to 0.35% for southern edge modules on a one-high configuration. The mismatch loss was found to depend strongly on albedo increasing by 5 times for frost.

We emphasize that our study is specific to mismatch within a single module (and not to module-to-module mismatch, which we expect to be more significant). The mismatch due to I_L variability would be compounded by mismatch due to cell-to-cell variation, and would be significantly higher for bifacial modules fixed nearer to the ground [2], [6] or for systems without backtracking. Mismatch loss could also increase due to shading from frames, poorly placed junction boxes, clamps, posts and other structures.

V References

[1] C. K. Lo, Y. S. Lim, and F. A. Rahman, "New integrated simulation tool for the optimum design of bifacial solar panel with reflectors on a specific site," *Renew. Energy*, vol. 81, pp. 293–307, 2015.

[2] U. A. Yusufoglu, T. M. Pletzer, L. J. Koduvelikulathu, C. Comparotto, R. Kopecek, and H. Kurz, "Analysis of the annual performance of bifacial modules and optimization methods," *IEEE J. Photovoltaics*, vol. 5, no. 1, pp. 320–328, 2015.

[3] A. Lindsay, M. Chiodetti, P. Dupeyrat, D. Binesti, E. Lutun, and K. Radouane, "Key elements in the design of bifacial PV power plants," in *31st EU PVSEC*, 2015, pp. 1764–1769.

[4] A. Lindsay *et al.*, "Modelling of single-axis tracking gain for bifacial PV systems," in *32nd EU PVSEC*, 2016, pp. 1610–1617.

[5] I. Shoukry, J. Libal, R. Kopecek, E. Wefringhaus, and J. Werner, "Modelling of Bifacial Gain for Stand-

alone and in-field Installed Bifacial PV Modules," *Energy Procedia*, vol. 92, pp. 600–608, 2016.

[6] C. A. Deline, S. A. Pelaez, P. Greenberg, J. Stein, and R. Kostuk, "Model and Validation of Single-Axis Tracking with Bifacial Photovoltaics," 2018.

[7] S. A. Pelaez, C. Deline, S. M. Macalpine, B. Marion, J. S. Stein, and R. K. Kostuk, "Comparison of bifacial solar irradiance model predictions with field validation," vol. 9, no. 1, pp. 82–88, 2019.

[8] S. A. Pelaez, C. A. Deline, P. Greenberg, J. Stein, and R. Kostuk, "Model and Validation of Single-Axis Tracking with Bifacial Photovoltaics," 2018.

[9] C. W. Hansen *et al.*, "A detailed model of rear-side irradiance for bifacial PV modules," in *43rd IEEE PVSC*, 2016, pp. 0138–0143.

[10] M. R. Vogt, T. Gewohn, K. Bothe, C. Schinke, and R. Brendel, "Impact of using spectrally resolved ground albedo data for performance simulations of bifacial modules," in *EU PVSEC*, 2018.

[11] M. A. Egido and E. Lorenzo, "Bifacial photovoltaic panels with sun tracking," *Int. J. Sol. energy*, vol. 4, no. 2, pp. 97–107, 1986.

[12] J. P. Oria and G. Sala, "A good combination: Tracking of the sun in polar axis and bifacial photovoltaic modules," vol. 5, no. 6, pp. 629–636, 1988.

[13] A. Mermoud and B. Wittmer, "PVSyst User's Manual." PVSyst SA, Satigny, Switzerland, 2014.

[14] U. A. Yusufoglu *et al.*, "Simulation of energy production by bifacial modules with revision of ground reflection," in *Energy Procedia*, 2014, pp. 389–395.

[15] G. J. M. Janssen, B. B. Van Aken, A. J. Carr, and A. A. Mewe, "Outdoor Performance of Bifacial Modules by Measurements and Modelling," *Energy Procedia*, vol. 77, pp. 364–373, Aug. 2015.

[16] D. Faiman, "Assessing the outdoor operating temperature of photovoltaic modules," *Prog. Photovoltaics Res. Appl.*, vol. 16, no. 4, pp. 307–315, 2008.

[17] M. D. Abbott, K. R. McIntosh, and B. Sudbury, "Optical loss analysis of pv modules," *EU PVSEC Proc.*, 2016.

[18] J. F. Hoelscher, F. Artigliere, S. Preis, and G. Stepanian, "A comparison of black, blue, and white backgrounds for high density solar modules," in *16th Photovoltaic Specialists Conference*, 1982, pp. 943–946.

[19] K. R. McIntosh, J. Jung, M. D. Abbott, and B. A. Sudbury, "Determination and evaluation of a backsheet's intrinsic reflectance," in *AIP Conference Proceedings*, 2018, vol. 1999, no. 1, p. 20018.

[20] A. M. Baldridge, S. J. Hook, C. I. Grove, and G. Rivera, "The ASTER spectral library version 2.0," *Remote Sens. Environ.*, vol. 113, no. 4, pp. 711–715, 2009.

[21] M. Chiodetti *et al.*, "PV bifacial yield simulation with a variable albedo model," in *32nd EU PVSEC*, 2016, pp. 1449–1455.

[22] A. Andreas and T. Stoffel, "NREL Solar Radiation Research Laboratory (SRRL): Baseline Measurement System (BMS); Golden, Colorado (Data); NREL Report No. DA-5500-56488.," 1981.

[23] R. Evans, M. Boreland, and M. A. Green, "A holistic review of mismatch loss: From manufacturing decision making to losses in fielded arrays," *Sol. Energy Mater. Sol. Cells*, vol. 174, pp. 214–224, 2018.

[24] M. R. Vogt, "Development of Physical Models for the Simulation of Optical Properties of Solar Cell Modules," Leibniz University, 2015.

[25] M. R. Vogt *et al.*, "Measurement of the optical constants of soda-lime glasses in dependence of iron content and modeling of iron-related power losses in crystalline Si solar cell modules," *IEEE J. Photovoltaics*, vol. 6, no. 1, pp. 111–118, 2016.

[26] M. R. Vogt *et al.*, "Optical constants of UV transparent EVA and the impact on the PV module output power under realistic irradiation," *Energy Procedia*, vol. 92, pp. 523–530, 2016.

[27] A. M. A.I. Golovashkin, "Optical properties of tin at helium temperaturs," *J. Exp. Theor. Phys.*, vol. 20, pp. 40–49, 1964.

[28] E. D. Palik, "Handbook of optical constants of solids," Orlando: Academic Press, 1985, pp. 397–400.

[29] P. Kumar, M. K. Wiedmann, C. H. Winter, and I. Avrutsky, "Optical properties of Al_2O_3 thin films grown by atomic layer deposition," *Appl. Opt.*, vol. 48, no. 28, p. 5407, Oct. 2009.

APPENDIX A

Tables A1 and A2 list the optical and electrical inputs used to simulate the bifacial module. These inputs are derived from datasheets and familiarity with modern commercial solar cells.

Table A1. Electronic inputs at 300 K. Assumed identical for all cells and diodes.

Property	Value	Notes
Cell connection	72 cells in series	
Bypass diode I_S	1 µA	m = 1.5 diode, three diodes, each across 24 cells.
Cell J_{01}	0.3 pA/cm^2	m = 1 diode
Cell J_{02}	0 nA/cm^2	m = 2 diode. Omitted because T-model is limited to one-diode. 5 nA/cm^2 is more typical.
Cell R_{Sh}	10 kΩ·cm^2	
Cell R_S	0.85 Ω·cm^2	Front grid: 0.28 Ω·cm^2 Rear grid: 0.24 Ω·cm^2 Non-grid: 0.33 Ω·cm^2 (which includ connectors in modules, internal Rs).

Table A2. Optical inputs for simulating the bifacial module. References give the source of each material's dispersive complex refractive index.

Property	Front	Rear
Glass morphology	Planar	Planar
Glass surface scattering	None	None
Glass ARC	110 nm of glass ARC [24]	None
Glass	2 mm of 0.05‰wt Fe_2O_3 glass [25]	2 mm of 0.05%wt Fe_2O_3 glass [25]
EVA	450 µm of UV transmissive EVA [26]	450 µm of UV transmissive EVA [26]
Ribbons	5 ribbons, 1 mm wide, 200 µm high, rectangular cross-section, Cu coated with Sn [27], specular.	5 ribbons, 1 mm wide, 200 µm high, rectangular cross-section, Cu coated with Sn [27], specular.
Fingers	102 Ag fingers [28], 20 µm high, 40 µm wide, rounded-rectangular profile, 1537 µm pitch, 80% Lambertian.	131 Al fingers [28], 20 µm high, 150 µm wide, rounded-rectangular profile, 1197 µm pitch, 80% Lambertian.
Busbars	5 busbars, 1 mm wide, same material and height as fingers	5 busbars, 1 mm wide, same material and height as fingers
Films	75 nm SiN_x with n = 2.09 at 632 nm [24]	20 nm ALD Al_2O_3 [29]
		100 nm SiN_x with n = 2.09 at 632 nm [24]
Cell morphology	53° random pyramids, 3 µm high	None
Cell surface scattering[a]	Phong model, α = 20	Phong model, α = 20
Collection efficiency	Fig. 16	Fig. 16
Cell bulk thickness[b]	177 µm	
Cell dimensions	6 x 12 cells, 15.68 cm square, 21 cm diameter; cell area of 244.46 cm^2.	
Cell separation	3 mm in x and y directions; unit-cell area of 255.4 cm^2.	
Additional space at edge of module	2.5 cm in x and y directions	
Module frame	None	
Module dimensions	100.85 cm × 196.76 cm; module area of 1.984 m^2.	

[a] Phong model simulates variability in pyramid angle, where α = 20 typically provides agreement with escape reflectance. Same scattering model used on rear for etched planar silicon.
[b] Excludes height of texture; hence total height is 180 µm.
[c] Spacing makes little difference to modules without a backsheet.

APPENDIX B

Weather and insolation data were downloaded from NREL databases [22]. Ambient temperature was downloaded for the tower dry bulb, wind velocity from 6' elevation, global intensity Φ_g from the CM3 (corr) database, global spectra $I_g(\lambda)$ from the SRRL WISER, direct insolation Φ_d from CHP1-1, and direct spectra $I_d(\lambda)$ from SRRL PGS-100.

The system is solved at 1 hourly intervals during the day. Where weather and insolation data are available in intervals less than 1 hour, we take the average of the intermediate points—except for zenith and azimuth angles, for which the value at the specific time is used.

Given the nature of the detector setup, the spectral data is somewhat piecemeal: $I_d(\lambda)$ is not available over the same wavelength range as $I_g(\lambda)$, and the ratio of integrated $I_g(\lambda)$ and Φ_g is not the same as the ratio of the integrated $I_d(\lambda)$ and Φ_d. We account for this in the following way: Negative values of Φ_g and Φ_d were set to zero. Where $\Phi_d \times \cos(\theta_{inc})$ exceeded Φ_g, Φ_d was scaled such that $\Phi_d \times \cos(\theta_{inc}) = \Phi_g$. $I_d(\lambda)$ was set to zero at $\lambda < 334$ because that data was not available (although this range is irrelevant due to these wavelengths being absorbed by the glass). $I_d(\lambda)$ was also not available at $\lambda > 1045.4$ nm; data for the range 1045–1250 nm was therefore assumed to be $I_d(\lambda) = I_g(\lambda) \times \Phi_d / \Phi_g$. Where the integral of $I_g(\lambda)$ exceeded Φ_g, $I_g(\lambda)$ was scaled uniformly at all λ such that the integral of $I_g(\lambda)$ equaled Φ_g; the same scaling was performed for $I_d(\lambda)$ where necessary.

The intention of the above procedure was to attain a realistic spectral intensity over the range $\lambda \leqslant 1250$ nm.

Finally, from 15-Sep to 18-Sep and from 26-Sep to 12-Oct, NREL's global spectral detector was temporarily deployed to measure the direct spectrum. We therefore neglect those days in the annual yield calculations.

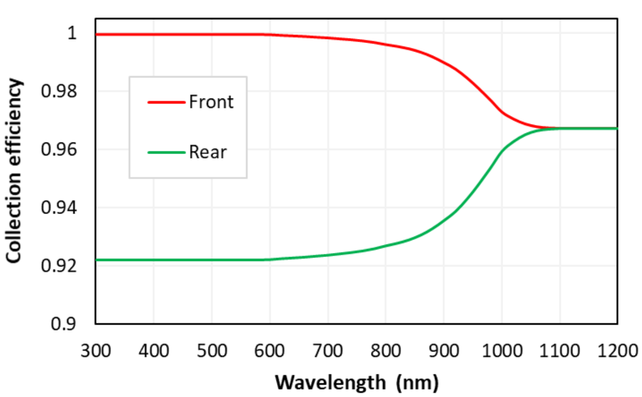

Fig. 16. Cell collection efficiency for front and rear illumination.